Check for updates

Original Research Article

JOURNAL OF THERMOPLASTIC COMPOSITE MATERIALS

Journal of Thermoplastic Composite Materials
2026, Vol. 0(0) 1–35
© The Author(s) 2026

Article reuse guidelines:
sagepub.com/journals-permissions
DOI: 10.1177/08927057261502569
journals.sagepub.com/home/jtc
Sage

Integration of carbon nanotubes in additively manufactured polylactic acid to develop creep and wear resistant nanocomposites

Kamil Feratoğlu[1] and İlyas İstif[2]

Abstract

This study experimentally investigates the mechanical, viscoelastic, and tribological behavior of carbon nanotube (CNT) reinforced polylactic acid (PLA) nanocomposites fabricated by fused deposition modeling (FDM). CNT-reinforced PLA filaments were used to produce test specimens, and the influence of CNT addition on tensile, creep, loading–unloading, and wear behavior was systematically evaluated. Tensile tests were conducted to determine the elastic–plastic deformation characteristics, while loading–unloading and creep experiments were employed to characterize the time-dependent viscoelastic and viscoplastic response of the nanocomposites. Tribological performance was assessed using pin-on-disk wear tests under different operating temperatures. The results demonstrate that CNT reinforcement significantly enhances the mechanical strength of PLA, reduces creep deformation, and increased the recovered strain energy while generally reducing the dissipated energy, indicating a more recoverable mechanical response. Furthermore, CNT addition leads to a noticeable reduction in wear rate and generally lowers the coefficient of friction, particularly at elevated temperatures. Scanning electron microscopy (SEM), combined with ImageJ-based 2D image analysis, was used to examine the interfilament void morphology and quantify the mean pore area and 2D pore area fraction of the printed specimens. The findings highlight the potential of CNT-reinforced PLA nanocomposites for tribological and structural applications in additively manufactured polymer components.

[1]Faculty of Engineering, Department of Mechanical Engineering, Kirklareli University, Kirklareli, Turkey
[2]Faculty of Machinery, Department of Mechanical Engineering, Yildiz Technical University, İstanbul, Turkey

Corresponding author:
Kamil Feratoğlu, Faculty of Engineering, Department of Mechanical Engineering, Kirklareli University, Kayali Campus, Merkez, Kirklareli 39020, Turkey.
Email: kamilferatoglu@klu.edu.tr

Keywords
Additive manufacturing, fused filament fabrication, nanocomposite polymers, creep behaviour, viscoelastic behaviour, wear behaviour

Introduction

Additive manufacturing (AM) enables the fabrication of complex geometries directly from digital models. Fused deposition modeling (FDM) is widely used among the various AM techniques. Although FDM is not generally cost-competitive with conventional mass-production processes such as injection molding at high production volumes, it offers advantages for prototyping, customized components, and low-volume production where tooling costs and geometric complexity are important considerations.[1–3]

The mechanical reliability of FDM-fabricated polymers is strongly influenced by their viscoelastic nature and by process-induced features such as internal voids, interlayer interfaces, and anisotropy.[3–7] These features affect not only time-dependent deformation but also fundamental static properties including stiffness, strength, and ductility. Orientation-dependent mechanical behavior is a well-established characteristic of orthotropic polymeric systems, in which the effective response varies with material direction and structural architecture. Similar direction-dependent thermo-mechanical behavior has also been demonstrated in numerical studies of orthotropic polymeric media.[8] Under sustained or repeated loading, they can promote creep deformation, incomplete recovery, dimensional instability and premature failure, particularly when mechanical loading is combined with elevated temperature or sliding contact.[9–11]

Nanocomposite filaments offer a possible route for improving the mechanical stability of FDM-fabricated polymers.[12–15] Carbon-based nanofillers, such as graphene, carbon black, and carbon nanotubes (CNTs), are particularly effective in restricting polymer chain mobility and enhancing stress transfer within the polymer matrix.[15,16] Carbon nanotubes (CNTs) are of particular interest because their high aspect ratio and large specific surface area can promote load transfer and restrict polymer-chain mobility when adequate dispersion and interfacial interaction are achieved. Such effects may increase stiffness and creep resistance, although excessive CNT content or agglomeration can also reduce ductility and limit reinforcement efficiency.[12,16,17] For PLA, this balance is especially relevant because neat PLA provides good processability but exhibits limited toughness and time-dependent mechanical stability in demanding service conditions. Accordingly, low CNT contents may provide a means of tailoring FDM-fabricated PLA for functional applications involving sustained loading and sliding contact.[12,14,16–19]

PLA was selected as the polymer matrix because of its widespread use in FDM, ease of processing, and suitability for producing complex functional components.[20,21] However, its relatively limited resistance to time-dependent deformation and wear restricts its use in applications involving sustained loading and sliding contact.[22,23] CNTs were therefore incorporated not to replace neat PLA in conventional low-cost applications, but to extend its functional performance through low reinforcement levels.[22,24,25] Owing to their high aspect ratio and stiffness CNTs can improve load transfer, creep

resistance, and tribological stability even at relatively low concentrations.[26–28] In the present study, CNT contents of 2–6 wt% were selected to investigate whether these improvements could be achieved without resorting to high filler loadings.[29,30] From an application perspective, such PLA/CNT nanocomposites may be relevant for FDM-fabricated functional parts subjected to sustained mechanical loading and repeated sliding contact, where the creep and wear limitations of neat PLA become critical.

The experimental program was designed to reproduce complementary aspects of the mechanical conditions encountered by FDM-fabricated functional components subjected to sustained loading and repeated sliding contact. Tensile testing was used to establish the baseline stiffness and strength of the PLA/CNT nanocomposites, whereas loading–unloading experiments were employed to assess deformation recovery and energy dissipation. Creep testing provided information on dimensional stability under sustained stress, while temperature-dependent pin-on-disk tests were used to evaluate friction and material loss under sliding contact. SEM-based microstructural and pore area analyses were further employed to relate these macroscopic responses to the internal structure of the printed materials. By integrating these measurements, the present study aims to clarify how CNT reinforcement influences the progression from bulk mechanical response to time-dependent deformation and ultimately to tribological performance.

Loading–unloading and creep experiments provide complementary information on elastic recovery, permanent deformation, energy dissipation, and time-dependent deformation.[17–19] These responses are particularly relevant for FDM components subjected to repeated mechanical contact, where viscoelastic deformation may alter the real contact area and consequently affect friction and wear. Although tensile properties of FDM-printed polymers have been extensively studied, comparatively fewer investigations have jointly considered loading–unloading behavior, creep response, and tribological performance.[12,16,18,19]

The tribological response of these materials is closely related to their bulk mechanical and viscoelastic behavior. During sliding, the surface is subjected to repeated normal and tangential loading, while creep and local deformation can influence frictional stability and material removal.[15] Despite previous studies on the tribological behavior of FDM-fabricated PLA composites,[15,31] the combined evaluation of creep, loading–unloading response, porosity, and temperature-dependent wear behavior in PLA/CNT nanocomposites remains limited.[12,18,19]

A preliminary stage of this research was previously reported in a conference paper.[32] The present study substantially extends that work by introducing a comprehensive tribological investigation, including temperature-dependent pin-on-disk wear and friction measurements, together with quantitative SEM/ImageJ-based 2D pore area analysis and strain-energy-density evaluation. Accordingly, the present work investigates the mechanical, viscoelastic, creep, and tribological behavior of FDM-fabricated PLA/CNT nanocomposites in an integrated framework. Tensile, loading–unloading, creep, and wear tests were combined with SEM characterization to clarify how CNT reinforcement influences deformation, structural integrity, and sliding performance. The overall objective is to establish the relationship between time-dependent mechanical response and

tribological behavior and thereby assess the suitability of PLA/CNT nanocomposites for FDM-fabricated components subjected to sustained and repeated contact loading.

Materials and Methods

Filament Preparation

Raw Materials. Polylactic acid (PLA) was supplied in granular form by Koluman Plastik A.Ş. According to the manufacturer's technical datasheet, PLA had a density of 1.24 g/cm^3 and a melt flow index of 22 g/10 min, which lies within the range typically reported for commercial PLA grades used in FDM/FFF filament production.[33,34] Prior to filament production, PLA granules were dried in a convection oven at 50°C for 2 h to eliminate moisture and ensure processing stability, consistent with common preprocessing protocols for PLA-based composites and nanocomposites.[15,35]

Carboxyl-functionalized (–COOH) multi-walled carbon nanotubes (MWCNTs) were supplied by Nanografi Nano Teknoloji A.Ş. According to the supplier specifications, the MWCNTs had lengths of 5–10 μm, diameters of 10–20 nm, and a purity of 96%, values comparable to those reported for MWCNTs used in PLA-based nanocomposites and hybrid systems.[29,36] The chemical functionalization of MWCNTs enhances interfacial adhesion between the CNTs and the PLA matrix, promoting more homogeneous dispersion and improved load transfer within the nanocomposite.[34] In particular, carboxylated or PLA-grafted MWCNTs show lower rheological percolation thresholds, improved dispersion, and stronger interfacial bonding compared with non-functionalized nanotubes, leading to higher stiffness and strength.[37] These improved CNT–matrix interactions are known to significantly influence the mechanical, viscoelastic, and, in some systems, tribological performance of PLA-based nanocomposites through enhanced stress transfer, restricted chain mobility, and increased energy dissipation capability.[15,33–35]

Pulverization and CNT Incorporation. To enhance interfacial adhesion between carbon nanotubes and the polymer matrix, PLA granules were first converted into powder form using a pulverization system equipped with a 500 mm diameter disc, a 55 kW motor, and a rotational speed of 5250 rpm, following solid-state pulverization concepts that promote CNT–polymer interfacial contact and dispersion in composite powders.[38] The powdered PLA was then mechanically mixed with carboxyl-functionalized multi-walled carbon nanotubes (MWCNTs) at CNT weight fractions of 2 wt%, 4 wt%, and 6 wt%. CNT contents above 6 wt% were not considered, as previous studies on PLA/MWCNT nanocomposites have been reported to exhibit CNT aggregation and deterioration of some mechanical properties at higher CNT contents, primarily due to agglomeration and reduced dispersion stability.[29]

Melt Blending. Melt blending of the PLA–CNT mixtures was carried out using a co-rotating twin-screw extruder (screw diameter: 18 mm, L/D ratio: 40; Polmak). The extrusion process for PLA–CNT nanocomposites was conducted at barrel temperatures

ranging from 155°C to 180°C, with screw rotation speeds between 20 and 30 rpm, depending on the CNT content. These processing conditions were selected to promote the distribution of CNTs within the PLA matrix while limiting thermal degradation of PLA, in accordance with previously reported twin-screw extrusion approaches for PLA/MWCNT nanocomposites.[39,40] The successful incorporation of CNTs was further supported by TGA, for which the calculated CNT contents were generally close to the corresponding nominal compositions. However, TGA provides information on the overall CNT content rather than its spatial distribution; therefore, homogeneous CNT dispersion at the nanoscale is not claimed in the present study.

Pelletization and Drying. Following melt blending, the filament-shaped semi-finished Neat PLA and PLA–CNT nanocomposite was pelletized using a granulation unit. The pellets were dried in a convection oven at 70°C for 4 h to remove residual moisture prior to filament extrusion, consistent with PLA–MWCNT filament fabrication routes where nanocomposite compounds are first melt compounded, granulated, and then re-extruded into filaments after controlled thermal conditioning/drying of the pellets before FDM/FFF processing.[29]

Filament Extrusion and Diameter Control. Dried pellets were then fed into a single-screw filament extrusion line to produce filaments with a nominal diameter of 1.75 mm suitable for FDM processing.[29] The extrusion line consisted of a single-screw extruder with three independently controlled heating zones, a water cooling tank, a haul-off unit for diameter control, and a winding system for filament collection. The barrel temperature profile for PLA–CNT nanocomposites was set to 170–180°C in the first zone, 170–180°C in the second zone, and 160–170°C in the third zone, depending on the CNT content. The screw rotation speed was maintained at 20 rpm during filament extrusion to ensure stable melt flow and consistent filament diameter. Cooling of the extruded filament was achieved using a water bath, followed by controlled drawing to obtain the target filament diameter.[41]

Process Overview and Filament Quality. The complete stages of PLA–CNT nanocomposite filament production are illustrated in Figure 1. As widely reported in the literature, homogeneous dispersion of nanofillers within the polymer matrix is critical for achieving improved mechanical and functional performance in FDM-fabricated components. To promote uniform CNT distribution, melt blending was performed using a co-rotating twin-screw extruder (screw diameter: 18 mm, L/D ratio: 40; Polmak). In addition to melt blending, the polymer granules were converted into powder form prior to CNT addition to enhance interfacial adhesion between the PLA matrix and the nanofillers, differing from conventional melt compounding approaches reported in the literature.

Thermal Characterization of PLA–CNT Filaments

Thermogravimetric Analysis. Thermogravimetric analysis was performed to evaluate the thermal degradation behavior of the produced PLA–CNT nanocomposite filaments and

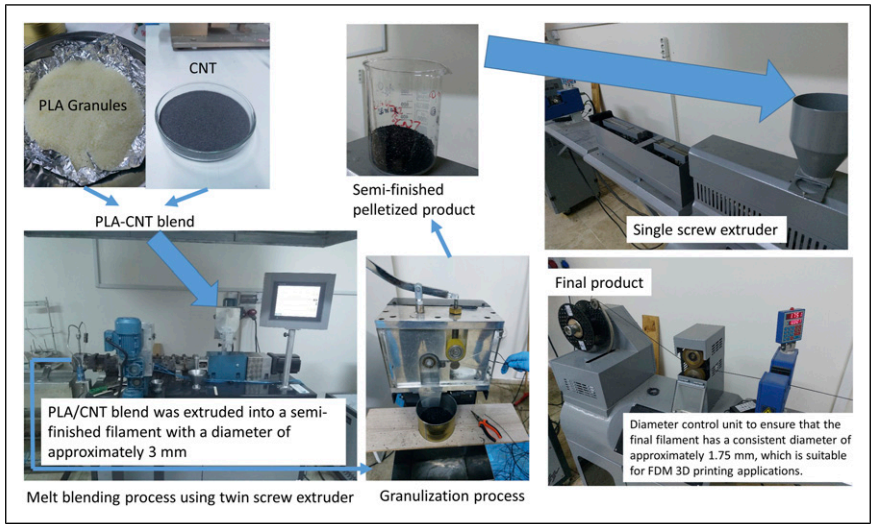


Figure 1. Schematic representation of PLA–CNT filament production including melt blending, pelletizing, granulation, and filament extrusion processes.

to verify the CNT content within the polymer matrix. Approximately 10 mg of filament samples were analyzed using a TA Instruments SDT 650 thermogravimetric analyzer. The measurements were carried out over a temperature range of 30°C to 900°C at a constant heating rate of 10°C/min.

To determine the residual CNT content after thermal degradation, temperature values below the complete decomposition temperature of the PLA matrix were selected. For PLA–CNT nanocomposites, residual mass measurements were taken at temperatures below 400°C to ensure that polymer degradation was complete while avoiding oxidation-related effects. The CNT weight fraction was calculated based on the residual mass remaining after thermal decomposition of the polymer matrix.

Differential Scanning Calorimetry (DSC). Differential scanning calorimetry (DSC) was conducted to determine the thermal transition behavior of the PLA–CNT nanocomposite filaments and to identify the glass transition temperature relevant for fused filament fabrication processing conditions. DSC measurements were performed using a TA Instruments Discovery DSC 250 system.

Approximately 10 mg of filament samples were tested under a nitrogen atmosphere to prevent oxidative effects. The analyses were carried out at a constant heating and cooling rate of 10°C/min over a temperature range of 30°C to 300°C. Heating–cooling cycles were applied to ensure thermal stability and repeatability of the measurements. The glass transition temperature was determined from the DSC thermograms following standard evaluation procedures.

Specimen Fabrication by Fused Filament Fabrication (FFF)

PLA–CNT nanocomposite specimens were fabricated by material extrusion (fused filament fabrication). During preliminary printing trials, nozzle clogging was observed, particularly at higher CNT loadings. This behavior is commonly associated with the agglomeration tendency of carbon nanotubes and increased melt viscosity of CNT-reinforced filaments. To ensure stable and continuous printing, a nozzle diameter of 0.8 mm was selected for the fabrication of all PLA–CNT specimens. All specimens were produced using a Creality CR-6 SE FFF printer. The printing parameters were optimized to prevent filament breakage and nozzle blockage while maintaining dimensional accuracy. Tensile test specimens were fabricated in accordance with ASTM D638–14 (Standard Test Method for Tensile Properties of Plastics, Type IV). The printing parameters used for the wear and mechanical test specimens are summarized in Table 1.

Printing Parameters. Printing parameters were selected to promote stable extrusion, low porosity, and strong interlayer bonding, which are known to govern tensile, flexural, and interlaminar properties in PLA-based AM parts. Nozzle temperature was increased with CNT content (200, 205, 210, and 210°C for 0, 2, 4, and 6 wt% CNT, respectively) to compensate for viscosity rise and preserve filament continuity. Based on DSC-derived glass transition temperatures, the build platform was set to 60°C, within the range reported to enhance first-layer adhesion and reduce warpage in PLA. Specimens were modeled in SolidWorks and sliced in Ultimaker Cura 4.10.0. The tensile specimens were fabricated using ±45° line and concentric raster configurations, whereas the wear specimens were produced using ±45° line, grid, and concentric infill patterns. The ±45° line raster provides alternating filament orientations and has been reported to reduce directional dependence compared with single-orientation raster configurations.[42,43] The bed was operated in an enclosed/ambient-controlled environment to limit thermal

Table 1. FFF printing parameters used for the fabrication of specimens for wear and mechanical tests.

Parameters	Wear	Mechanical
Infill types	Grid, line (−45°, +45°), concentric	Line (−45°, +45°), concentric
Geometry	Pin Diameter: 10 mm Height: 20 mm	ASTM D638-14 (Type IV tensile specimen)
Bed temperature	60°C	
Nozzle temperatures	200°C (Neat PLA), 205°C (PLA-wt%2 CNT), 210°C (PLA-wt%4 and wt% 6 CNT)	
Nozzle diameter	0.8 mm	
Layer height	0.2 mm	
Infill density	100%	

gradients that can deteriorate interlayer adhesion. The printing parameters are summarized in Table 1.

SEM Analysis and 2D Pore Area Quantification

Scanning electron microscopy (SEM) was used to examine the microstructural features and interfilament void morphology of the FFF-fabricated PLA–CNT nanocomposite specimens. SEM images were acquired from the cross-sectional surfaces of specially prepared specimens designed to examine interfilament contact morphology and local void formation between adjacent deposited roads. Quantitative analysis of pore area density was performed using the open-source ImageJ software. SEM images were first converted to grayscale and subsequently transformed into binary images using a thresholding procedure. In the thresholding process, pixel intensities below a selected threshold value were classified as pores, while pixels above the threshold were identified as solid material. Lower and upper threshold limits were defined manually to ensure accurate differentiation between pores and the polymer matrix. Following binarization, the pore area fraction was calculated as the ratio of the total pore area to the analyzed image area. This approach enabled a quantitative comparison of the local 2D pore area fractions among PLA–CNT nanocomposites with different CNT contents.

A representative pore area analysis procedure performed on the SEM cross-sectional images is illustrated in Figure 2. For the analysis, a rectangular region of interest (ROI) was selected from the interfilament zone of the printed specimen, where the voids formed between adjacent deposited roads were clearly visible. The selected ROI was converted to 8-bit grayscale and segmented by thresholding in ImageJ in order to distinguish the pore regions from the polymer matrix. After thresholding, the identified pores were isolated and quantified using the Analyze Particles function. The representative ROI analysis revealed the presence of 8 distinct pores within the selected region. Based on the ImageJ analysis, the total pore area was approximately 3.07×10^4 μm^2, while the mean single-pore cross-sectional area was approximately 3.83×10^3 μm^2. The corresponding 2D pore area fraction was 3.71%, calculated according to equation (1). These results indicate that the voids in the printed structure are mainly concentrated along the interfilament boundaries and are associated with incomplete fusion between neighboring extruded filaments during the FFF process.

$$Pore\ Area\ Density\ (\%) = \frac{Total\ Pore\ Area}{Analyzed\ ROI\ Area} x100 \tag{1}$$

To improve the repeatability and comparative reliability of the pore morphology analysis, the ImageJ-based measurements were performed on multiple regions and specimens for each material composition. For each printed specimen, two different regions of interest (ROI) were selected from comparable interfilament zones in the cross-sectional SEM images where printing-induced inter-road voids were observed. The pores within each selected ROI were identified through threshold segmentation and quantified

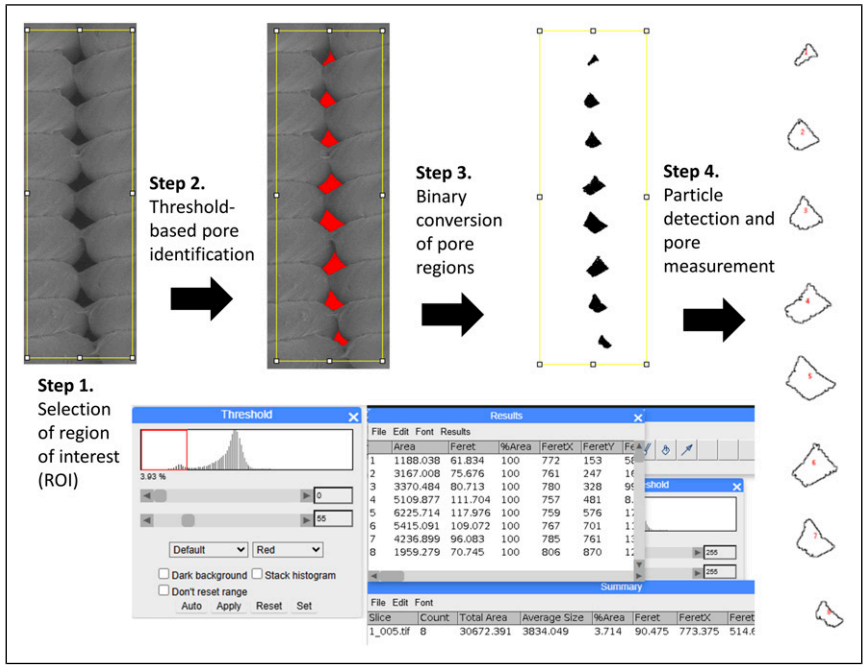


Figure 2. Procedure used for pore morphology analysis using ImageJ software.

using the Analyze Particles function in ImageJ. For every material composition, three specimens with identical printing parameters and composition were analyzed. Approximately eight pores were measured within each ROI, resulting in approximately 48 individual pore measurements per material (8 pores × 2 regions × 3 specimens). The mean pore area and associated statistical parameters were calculated from these measurements for comparative evaluation of the PLA–CNT compositions. Because the analysis was performed on two-dimensional SEM cross-sections, the measured pore area and pore area fraction were considered 2D descriptors of the local void morphology and were not interpreted as direct measurements of three-dimensional pore volume or global volumetric porosity. The multi-region and multi-specimen approach was therefore employed to reduce the influence of local microstructural variations and to improve the reproducibility of the comparative 2D analysis.

Mechanical and Tribological Testing

The mechanical, viscoelastic, creep, and tribological behaviors of the FFF-fabricated PLA–CNT nanocomposites were systematically investigated through a series of standardized experimental tests. The experimental setups used for mechanical and tribological testing are presented in Figures 3 and 4. The mechanical tests were performed using a Shimadzu universal testing machine (model AGS-X) equipped with a 10 kN load



Figure 3. Universal testing machine (Shimadzu AGS-X) used for mechanical tests.

cell. Uniaxial tensile tests were conducted to determine the basic mechanical properties of the printed specimens, including tensile strength and deformation behavior under different strain rates. Loading–unloading tests were carried out to evaluate the visco-elastic response and hysteretic energy dissipation behavior of the materials. In addition, creep experiments were performed to investigate the time-dependent deformation

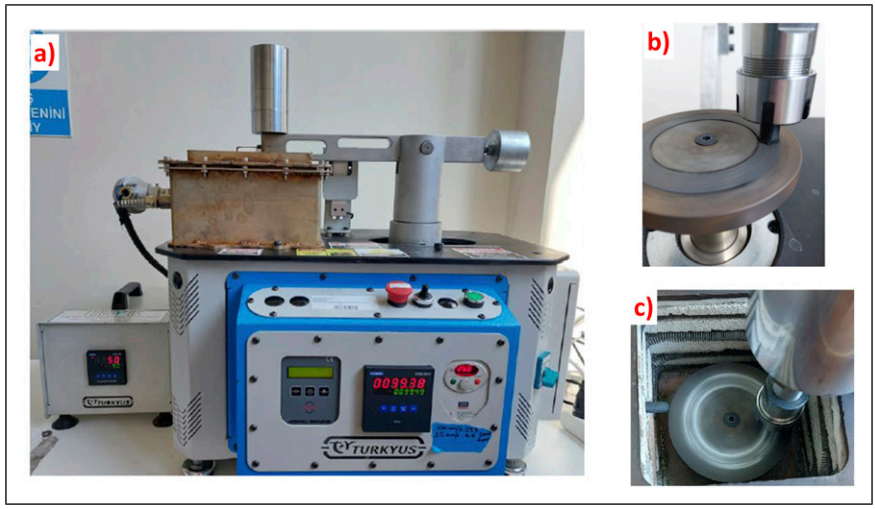


Figure 4. Experimental setup used for the pin-on-disk wear tests. (a) Overall view of the pin-on-disk tribometer integrated with a temperature control system, (b) close-up view of the sliding contact under room-temperature conditions without heating, and (c) close-up view of the wear test configuration with the heating module used for elevated-temperature experiments.

behavior under sustained loading. Finally, dry sliding wear tests were conducted using a pin-on-disk tribometer to assess the tribological performance of the nanocomposites under different temperature conditions.

Uniaxial Tensile Testing. Uniaxial tensile tests were conducted to evaluate the mechanical behavior of FFF-fabricated PLA–CNT nanocomposite specimens. All tensile specimens were fabricated in accordance with ASTM D638 (Type IV). A gauge length of 25 mm was used during testing. To investigate the strain-rate-dependent mechanical response of the PLA–CNT nanocomposites, tensile tests were carried out at nominal strain rates of 1×10^{-3} s^{-1} and 1×10^{-4} s^{-1}, corresponding to crosshead speeds of 1.5 mm/min and 0.15 mm/min, respectively. At least three specimens were tested for each condition, and the average values were reported.

Loading–Unloading Testing. Quasi-static loading–unloading tests were performed to investigate the recoverable and dissipative mechanical response of the FFF-fabricated PLA–CNT nanocomposite specimens. Tensile specimens manufactured in accordance with ASTM D638 were used for all loading–unloading experiments The tests were conducted at room temperature using maximum strain levels of 3% and 5%. These strain levels were selected to characterize the deformation recovery, hysteresis behavior, and strain-energy partitioning of the materials without assuming a purely elastic response. To evaluate the effect of strain rate, loading–unloading tests were performed at nominal

strain rates of 1×10^{-3} s^{-1} and 1×10^{-4} s^{-1}, corresponding to crosshead speeds of 1.5 mm/min and 0.15 mm/min, respectively.

The hysteresis loops obtained from the loading–unloading cycles were analyzed to quantify the mechanical energy stored, recovered, and dissipated during deformation. As schematically illustrated in Figure 5, the stored strain energy density ($U_{loading}$) was determined from the area under the loading segment of the stress–strain curve, while the recovered strain energy density ($U_{unloading}$) was calculated from the area under the unloading segment. The difference between these two quantities represents the energy dissipation density (U_{diss}), which characterizes the viscoelastic energy loss occurring during the deformation. The strain energy density was determined by numerical integration of the stress–strain curves according to:

$$U = \int \sigma \, d\varepsilon, \tag{2}$$

and the dissipated energy was obtained as:

$$U_{diss} = U_{loading} - U_{unloading}. \tag{3}$$

The integration of the stress–strain curves and calculation of the energy densities were performed using the numerical integration tool in OriginPro 2021. For each testing condition, at least three specimens were tested and the average responses were reported.

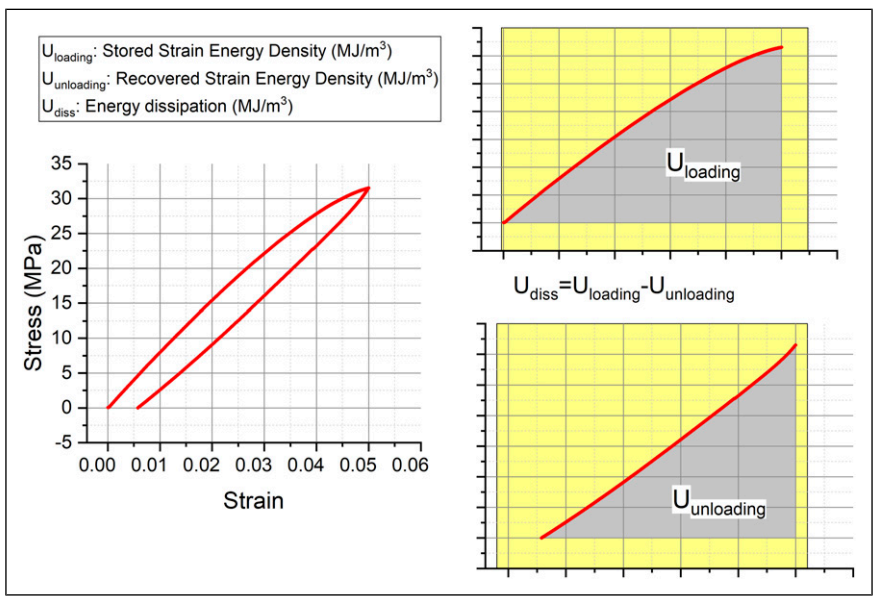


Figure 5. Methodology used to quantify loading, recovered, and dissipated strain energy densities from quasi-static loading–unloading tensile tests.

Creep Testing. Creep tests were conducted to evaluate the time-dependent deformation behavior and durability of the FFF-fabricated PLA–CNT nanocomposite specimens. The experiments were carried out in accordance with ASTM D2990–17 under constant stress conditions at room temperature. Rectangular specimens with dimensions of 6 × 3.2 × 25 mm^3 were used for the creep experiments. Prior to testing, stress levels were selected to ensure that deformation remained within the linear viscoelastic regime. Accordingly, a constant tensile stress of 16.25 MPa was applied, and creep deformation was recorded over a duration of 10,000 s (approximately 2.78 h). Strain data were continuously monitored as a function of time. To ensure the reliability and repeatability of the results, each creep test condition was repeated at least three times using different specimens.

The creep behavior was evaluated in terms of creep compliance, which describes the strain response of a material under a constant applied stress. Creep compliance $J(t)$ was calculated as the ratio of the time-dependent strain $\varepsilon(t)$ to the applied stress σ:

$$J(t) = \varepsilon(t)/\sigma, \tag{4}$$

When plastic deformation does not occur, the total isothermal creep compliance J_{tot} consists of two components: the instantaneous elastic compliance J_{el} and the time-dependent viscoelastic compliance $J_{ve}(t)$. Accordingly, the total creep compliance can be expressed as:

$$J_{tot}(t) = J_{el} + J_{ve}(t). \tag{5}$$

Wear Testing. Dry sliding wear tests were conducted to evaluate the tribological behavior of FFF-fabricated PLA–CNT nanocomposite specimens. The experiments were performed using a pin-on-disk tribometer in accordance with the ASTM G99 standard. The experimental setup of the pin-on-disk tribometer equipped with a heating module is shown in Figure 4.

An AISI 1040 steel disk with a surface roughness of Ra = 3.2 μm and a hardness of 211 HV (Vickers hardness) was used as the counterface material. The surface roughness of the steel disk was measured using an optical profilometer. Prior to each test, both the disk and specimen surfaces were cleaned with acetone to remove contaminants. The mass of each specimen was measured before and after the wear tests using a balance with an accuracy of 1×10^{-4} g. During the experiments, the tangential friction force was monitored using a load cell and recorded continuously through a data acquisition system to determine the coefficient of friction. Wear tests were conducted under a normal load of 40 N, a sliding speed of 1 m s^{-1}, and a total sliding distance of 3000 m. The cylindrical pin specimens had a diameter of 10 mm and a height of 20 mm. To investigate the influence of temperature on tribological performance, the experiments were carried out at room temperature, 30°C, and 40°C using a heating module integrated into the tribometer. The main parameters used in the wear experiments are summarized in Table 2.

The wear resistance of the specimens was evaluated based on the mass loss measured before and after each pin-on-disk test. The measured mass loss, Δm, was converted into volumetric material loss by considering the density of the corresponding material:

Table 2. Experimental parameters used in the pin-on-disk wear tests.

Parameter	Value
Counterface material	AISI 1040
Disk hardness (HV)	211
Disk surface roughness (Ra, μm)	3.2
Normal load (N)	40
Sliding distance (m)	3000
Sliding speed (m/s)	1
Pin diameter (mm)	10
Pin height (mm)	20
Test temperatures (°C)	Room temperature (22±2°C), 30°C, 40°C

$$V = \frac{\Delta m}{\rho}, \tag{6}$$

where V is the wear volume, Δm is the mass loss, and ρ is the material density. The specific wear rate was then calculated by normalizing the wear volume with respect to the applied normal load and the total sliding distance, according to the commonly used volumetric wear-rate relationship[44]:

$$K = \frac{V}{F_N L} = \frac{\Delta m}{\rho F_N L}. \tag{7}$$

where K is the specific wear rate [kg/kg.m^{-3}.N.m] is the applied normal load (N), and L is the total sliding distance (m). This formulation enables the wear performance of the different PLA/CNT compositions to be compared independently of the applied load and sliding distance.

Results and Discussion

This section presents the mechanical, viscoelastic, creep, and tribological behavior of the FFF-fabricated PLA–CNT nanocomposite specimens. The influence of carbon nanotube (CNT) reinforcement, printing parameters, and testing conditions on the deformation and wear characteristics of the material was systematically analyzed. First, the mechanical response of the specimens was evaluated through uniaxial tensile tests conducted at different strain rates. Subsequently, loading–unloading experiments were performed to investigate the viscoelastic and hysteretic behavior associated with energy dissipation during the defortmation. The time-dependent deformation characteristics of the materials were then analyzed through creep tests under constant stress conditions. Finally, dry sliding wear experiments were conducted to evaluate the tribological performance of the PLA–CNT nanocomposites under different temperature conditions.

Thermal Characterization (DSC/TGA)

Thermogravimetric Analysis. Thermogravimetric (TGA) and derivative thermogravimetric (DTG) curves of neat PLA, CNT, and PLA–CNT nanocomposite filaments are presented in Figure 6. As observed in the thermograms, neat PLA exhibits a single-stage thermal degradation behavior, with the main decomposition occurring in the temperature range of approximately 300–370°C. The DTG curve of neat PLA shows a sharp degradation peak around 340–350°C, corresponding to the rapid thermal decomposition of the polymer matrix. In contrast, CNT demonstrates significantly higher thermal stability, with minimal mass loss up to approximately 600°C.

The incorporation of CNT into the PLA matrix does not significantly change the overall degradation mechanism of PLA; however, an increase in the residual mass is clearly observed with increasing CNT content. This behavior is attributed to the high thermal stability of CNTs, which remain as residue after the polymer matrix has decomposed. To estimate the CNT content in the nanocomposites, the residual mass values obtained from the TGA thermograms were analyzed at selected temperatures below 400°C to ensure that the PLA matrix had largely decomposed while minimizing possible oxidation effects. The residual mass percentages of neat PLA and PLA–CNT nanocomposites at 375°C, 390°C, and 400°C are summarized in Table 3. As shown in the table, the residual mass increases with increasing CNT loading, confirming the successful incorporation of CNTs into the PLA matrix.

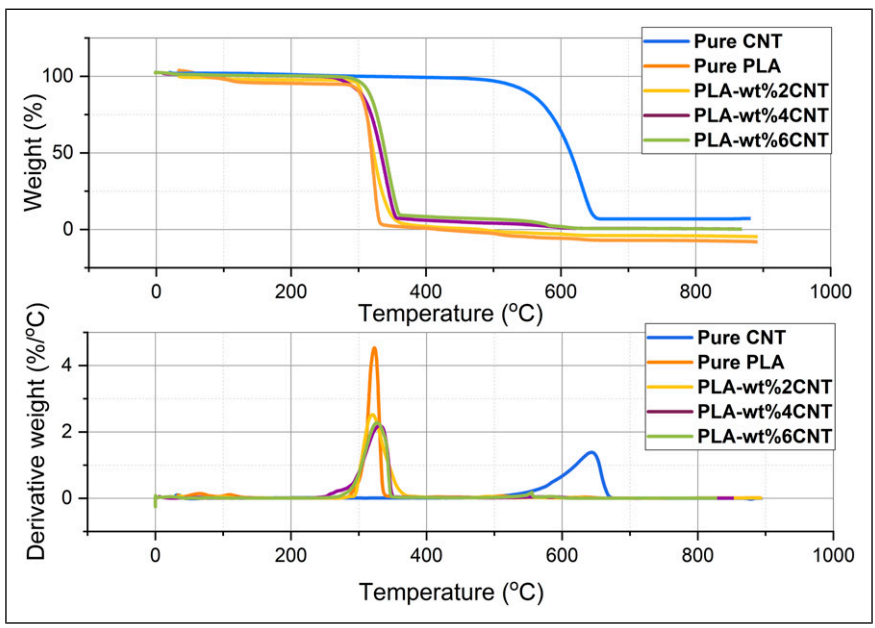


Figure 6. TGA and DTG thermograms of neat PLA, CNT, and PLA–CNT nanocomposite filaments.

Table 3. Residual mass values and estimated CNT contents of PLA–CNT nanocomposites obtained from TGA thermograms.

Material	Residual mass at 375°C (%)	Residual mass at 390°C (%)	Residual mass at 400°C (%)	Nominal CNT content (%)	Calculated CNT content at 375°C (%)	Calculated CNT content at 390°C (%)	Calculated CNT content at 400°C (%)
Neat PLA	6.19	3.29	2.98	–	–	–	–
PLA–2 wt% CNT	8.31	5.04	4.61	2	2.12	1.75	1.63
PLA–4 wt% CNT	10.44	8.02	7.41	4	4.25	4.73	4.43
PLA–6 wt% CNT	12.06	9.64	8.88	6	5.87	6.35	5.90

The CNT weight fraction in the nanocomposites was calculated based on the difference between the residual mass of the composite and that of neat PLA after thermal degradation, as expressed in equation (8). The calculated CNT contents were generally close to the nominal compositions of 2 wt%, 4 wt%, and 6 wt%, supporting the successful incorporation of CNTs and confirming that the bulk compositions of the produced nanocomposites were consistent with the intended CNT loadings.

$$\mathrm{CNT}(\mathrm{wt}\%) = \text{Residual mass of composite}(\mathrm{wt}\%) - \text{Residual mass of neat PLA}(\mathrm{wt}\%). \tag{8}$$

Differential Scanning Calorimetry (DSC). The DSC thermograms of neat PLA and PLA–CNT nanocomposites are presented in Figure 7. The thermal transitions observed in the DSC curves provide insight into the influence of CNT reinforcement on the thermal behavior of the PLA matrix. As observed in the thermograms, neat PLA exhibits a glass transition temperature (Tg) at approximately 57.4°C. After the incorporation of CNTs, the Tg values remain nearly unchanged, being 57.5°C, 56.8°C, and 57.5°C for PLA–2 wt % CNT, PLA–4 wt% CNT, and PLA–6 wt% CNT, respectively. The minimal variation in Tg indicates that the addition of CNTs did not cause a pronounced shift in the segmental mobility of the PLA chains. Similar observations have been reported in PLA-based nanocomposites reinforced with carbon nanofillers, where the glass transition temperature remains relatively stable due to limited interaction between the polymer chains and the filler surfaces. The DSC curves also reveal a crystallization peak in the temperature range of approximately 100–120°C, which becomes slightly more pronounced with increasing CNT content. This behavior suggests that CNTs act as

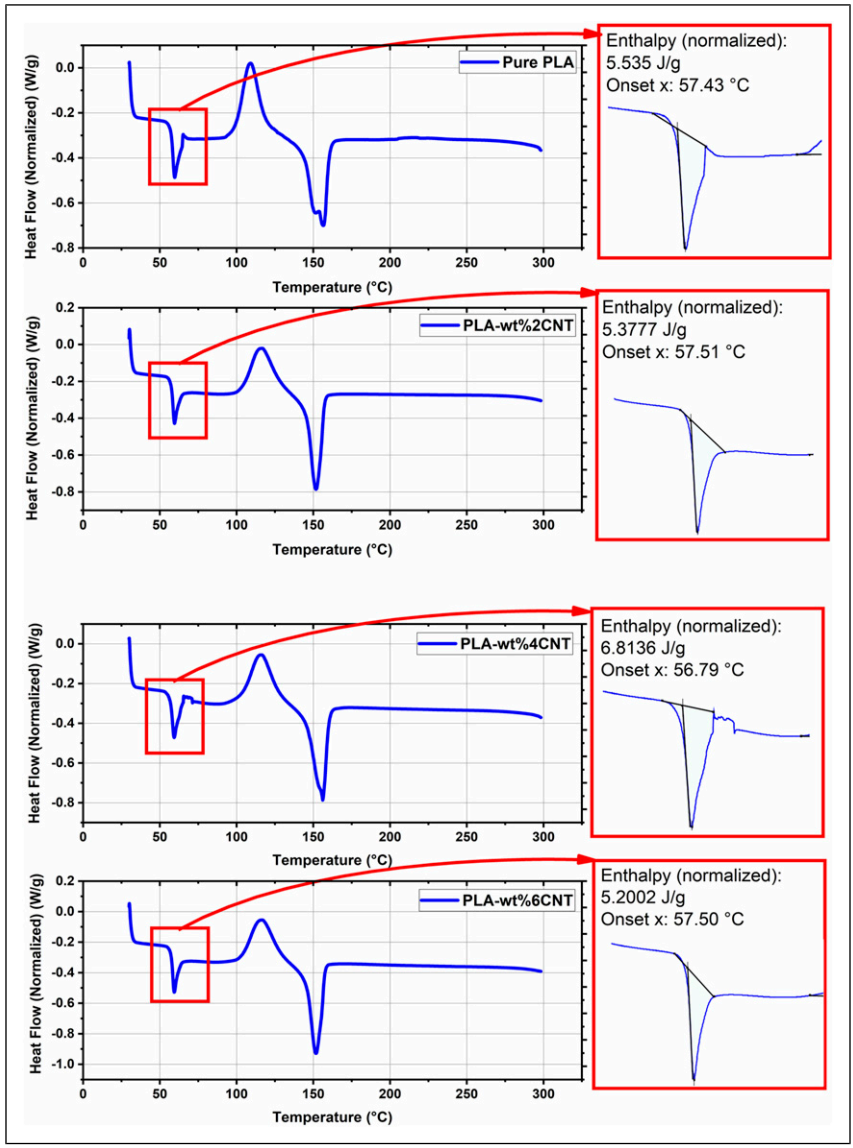


Figure 7. DSC thermograms of neat PLA and PLA–CNT nanocomposite filaments showing glass transition, crystallization, and melting behavior.

heterogeneous nucleating agents, facilitating the crystallization of the PLA matrix. The presence of nanoscale fillers such as CNTs provides additional nucleation sites that promote crystal formation during thermal treatment. Similar nucleation effects of CNTs in PLA matrices have been reported in previous studies, where CNT reinforcement

enhances the crystallization rate by providing energetically favorable sites for crystal growth.

In addition, the melting peak of PLA is observed at approximately 150–160°C for both neat PLA and PLA–CNT nanocomposites. The position of the melting peak remains nearly unchanged with increasing CNT content, indicating that the crystalline structure of PLA is largely preserved after CNT incorporation. This behavior suggests that while CNTs influence the nucleation process during crystallization, they do not significantly alter the crystal structure or melting behavior of PLA. Similar findings have been reported in the literature, where CNT-filled PLA nanocomposites exhibit enhanced crystallization kinetics without substantial changes in melting temperature.

The normalized enthalpy values obtained from the selected transition region were 5.54 J/g for neat PLA, 5.38 J/g for PLA–2 wt% CNT, 6.81 J/g for PLA–4 wt% CNT, and 5.20 J/g for PLA–6 wt% CNT, indicating slight variations in thermal energy absorption with CNT incorporation. Overall, the DSC results demonstrate that CNT reinforcement slightly modifies the crystallization behavior of PLA by acting as a nucleating agent while preserving the fundamental thermal transition characteristics of the polymer matrix.

Fabricated Specimens, Microstructural Characterization, and 2D Pore Area Analysis of FFF-Fabricated PLA–CNT Nanocomposites

Figure 8 presents the as-fabricated FFF tensile specimens produced with line (±45°) and concentric raster patterns, as well as the cylindrical wear specimens fabricated using line (±45°), concentric, and grid infill configurations. Cylindrical specimens having a diameter of 10 mm and a height of 20 mm were fabricated by FFF and used in the pin-on-disk wear tests. The printed specimens exhibited well-defined geometries and stable filament deposition, indicating that the selected printing parameters enabled consistent extrusion during the fabrication process. The tensile specimens produced according to the ASTM D638 Type IV geometry maintained dimensional accuracy and uniform filament alignment along the gauge section. No severe printing defects such as incomplete extrusion or filament discontinuity were observed in the fabricated PLA–CNT specimens.

SEM Analysis and Interlayer Morphology. The microstructural characteristics of the PLA–CNT specimens were further examined using scanning electron microscopy (SEM). The SEM images of the printed specimens are presented in Figure 9, where (a) corresponds to neat PLA, while (b), (c), and (d) represent PLA–2 wt% CNT, PLA–4 wt% CNT, and PLA–6 wt% CNT composites, respectively. The micrographs clearly reveal the layered structure typical of fused filament fabrication. The deposited filaments form distinct raster patterns, and small voids are visible between adjacent filaments due to incomplete fusion during the deposition process. Comparison of the SEM images indicates that the dimensions of the interfilament void regions generally decrease following CNT incorporation. This observation is consistent with the quantitative 2D pore area analysis presented in Figure 9. However, the observed differences in void morphology should not be attributed solely to CNT incorporation. Interfilament contact and void formation in

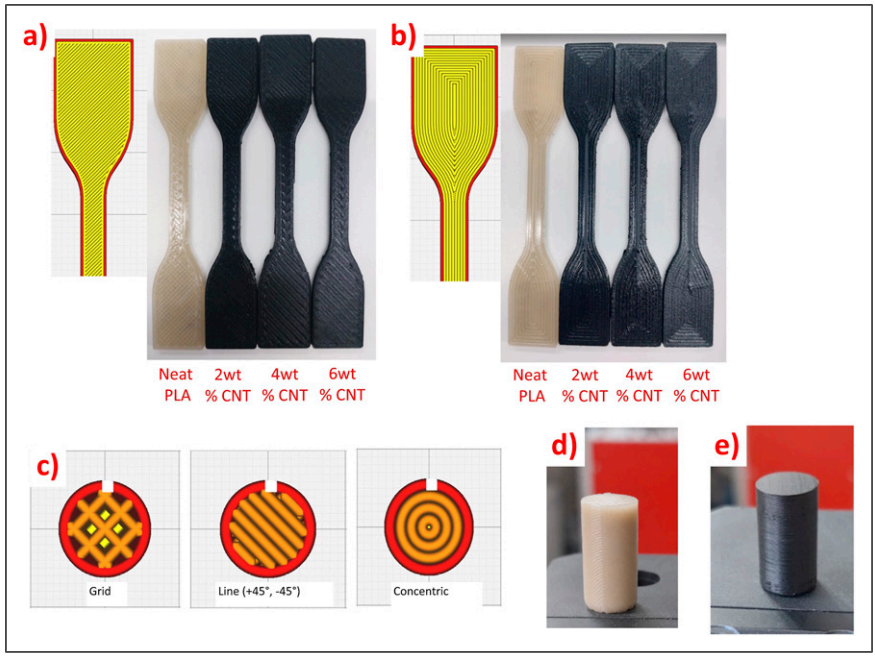


Figure 8. Printing configurations and representative FFF-fabricated specimens used in the mechanical and wear tests: (a) ±45° line raster pattern and corresponding tensile specimens of neat PLA and PLA–CNT nanocomposites, (b) concentric infill pattern and corresponding tensile specimens, (c) schematic representation of the grid, line (±45°), and concentric infill patterns used for the wear specimens, and representative cylindrical pin-on-disk specimens fabricated from (d) neat PLA and (e) PLA–CNT nanocomposite.

FFF are also influenced by processing conditions governing polymer melting, extrusion, deposition, and fusion, including nozzle temperature, material flow rate, printing speed, nozzle geometry, and thermal conditions during deposition. Therefore, the microstructural differences observed in the present study are interpreted as the combined result of material composition and the associated processing conditions rather than as direct evidence of improved interlayer adhesion caused by CNT addition. Previous studies have similarly demonstrated the important role of extrusion and deposition parameters in controlling inter-road bonding and defect formation in FFF-fabricated polymers.[45]

The pore morphology of the FFF-fabricated PLA–CNT nanocomposites was quantitatively evaluated using the ImageJ-based image analysis procedure described previously. The results are summarized in Figure 9, which presents the variation of mean single-pore cross-sectional area and pore area density for the different material compositions. The mean single-pore cross-sectional area decreased significantly with the addition of CNT reinforcement into the PLA matrix. The neat PLA specimen exhibited the largest pore area, with an average value of approximately 5700 μm^2, indicating relatively large interfilament voids formed during the FFF process. When 2 wt% CNT

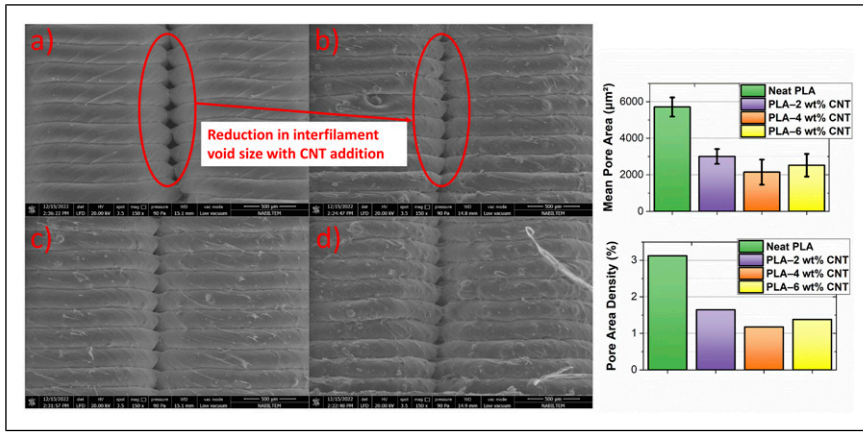


Figure 9. Cross-sectional SEM morphology and quantitative analysis of interfilament voids in FFF-fabricated PLA–CNT nanocomposites: (a) neat PLA, (b) PLA–2 wt% CNT, (c) PLA–4 wt% CNT, and (d) PLA–6 wt% CNT. The corresponding bar charts present the mean pore area and 2D pore area density determined from ImageJ analysis.

was incorporated into the polymer matrix, the average pore area decreased to approximately 3000 μm^2, suggesting improved melt flow behavior and enhanced contact between adjacent deposited filaments. The smallest pore area was observed for the PLA–4 wt% CNT composite, with a value close to 2100 μm^2, indicating a more compact internal structure and improved interfilament bonding during deposition. However, a slight increase in the mean pore area was observed for the PLA–6 wt% CNT specimen, which can be attributed to the increased viscosity of the polymer melt at higher CNT concentrations, potentially limiting filament spreading and reducing the efficiency of interlayer fusion.

A similar trend can be observed in the pore area density values. The neat PLA specimen exhibited the highest pore area density of approximately 3.1%, while the incorporation of CNT nanoparticles significantly reduced the pore area density of the printed structures. The density decreased to approximately 1.6% for the PLA–2 wt% CNT composite and reached the lowest value of around 1.2% for the PLA–4 wt% CNT specimen, indicating improved packing of the deposited filaments and reduced void formation. At higher CNT content (6 wt% CNT), the pore area density slightly increased to about 1.4%, which is consistent with the pore area results and suggests that excessive nanoparticle loading may negatively influence melt flow behavior during the FFF process.

The SEM cross-sectional images further support these quantitative observations, revealing that most voids are located along the interfilament boundaries, which are typical defect regions in FFF-printed structures. These voids originate primarily from incomplete fusion between neighboring extruded filaments during deposition. The addition of CNT nanoparticles appears to improve the internal microstructural integrity of the printed parts by promoting better filament packing and reducing the size and number of inter-road voids.

From a tribological perspective, the reduction in pore size and overall pore area density is particularly beneficial for improving the mechanical stability and wear resistance of the printed structures. In tribological contacts, pores and internal voids can act as stress concentration sites, which facilitate crack initiation and accelerate material removal during sliding. Therefore, the observed decrease in both pore area and pore area density with CNT addition is expected to enhance the load-bearing capacity of the material and improve its resistance to wear. The PLA–4 wt% CNT composite, which exhibited the lowest pore area density and smallest pore size, can therefore be considered the most structurally compact material among the studied compositions. This improved microstructural compactness is expected to contribute positively to the tribological performance of the PLA–CNT nanocomposites.

Tensile Behaviour

The tensile behavior of the FFF-fabricated PLA–CNT nanocomposites was evaluated for different CNT contents, raster orientations, and strain rates. Representative stress–strain curves are presented in Figure 10. Incorporation of CNT reinforcement significantly

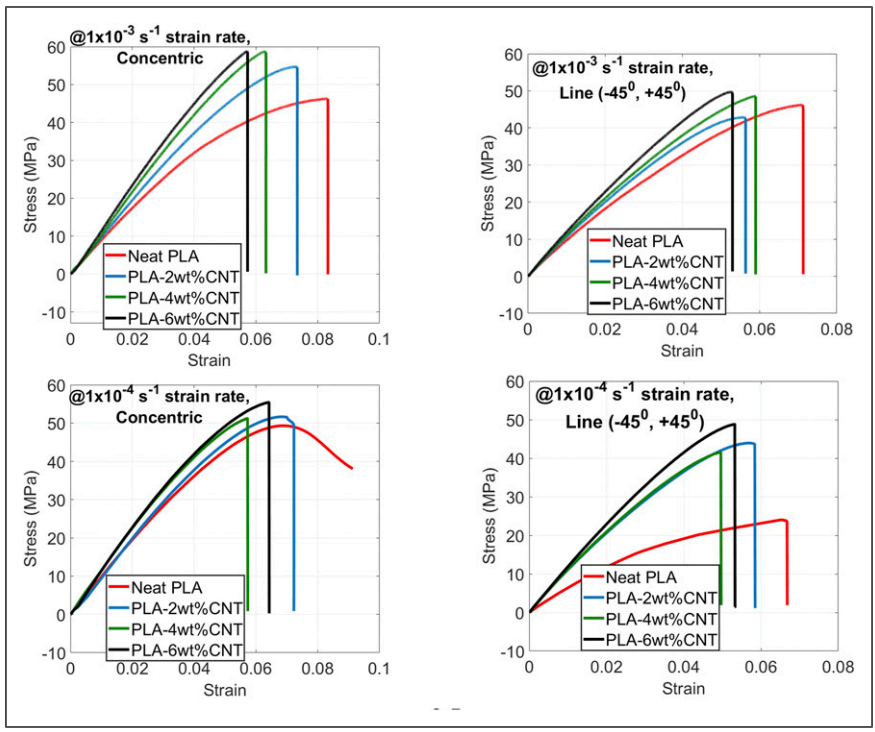


Figure 10. Tensile stress–strain curves of neat PLA and PLA–CNT nanocomposites fabricated with concentric and ±45° line infill patterns at strain rates of 1×10^{-3} and 1×10^{-4} s^{-1}.

increases both the tensile strength and elastic modulus compared to neat PLA. The PLA–CNT composites exhibit higher stiffness and improved load-bearing capacity due to the reinforcing effect of carbon nanotubes within the polymer matrix. Increasing the strain rate results in higher tensile strength values for all compositions. This behavior is typical for polymer-based materials and can be attributed to the rate-dependent viscoelastic response of the PLA matrix. At higher strain rates, the molecular chains have less time to rearrange, leading to increased resistance to deformation and therefore higher tensile strength.

The combined influence of CNT content, raster orientation, and strain rate on the tensile properties is summarized in Figure 11. For the concentric configuration at a strain rate of 1×10^{-3} s^{-1}, the tensile strength increased from 46.27 MPa for neat PLA to 54.68, 58.69, and 58.81 MPa for PLA–2 wt% CNT, PLA–4 wt% CNT, and PLA–6 wt% CNT, corresponding to increases of approximately 18.2%, 26.8%, and 27.1%, respectively. At 1×10^{-4} s^{-1}, the corresponding increases were more moderate, amounting to approximately 4.7%, 3.9%, and 12.4%. For the ±45° line configuration at 1×10^{-3} s^{-1}, the addition of 2 wt% CNT resulted in a 7.2% decrease in tensile strength, whereas the incorporation of 4 and 6 wt% CNT increased the tensile strength by approximately 6.7% and 7.6%, respectively. At 1×10^{-4} s^{-1}, a considerably stronger effect was observed. Compared with the tensile strength of neat PLA (21.12 MPa), the values obtained for PLA–2 wt% CNT, PLA–4 wt% CNT, and PLA–6 wt% CNT corresponded to increases of approximately 108.1%, 96.6%, and 131.2%, respectively. These findings indicate that the effect of CNT incorporation on tensile strength is not strictly monotonic and depends strongly on both strain rate and filament-path architecture.

A more consistent CNT-dependent trend was observed for the elastic modulus. For the concentric specimens tested at 1×10^{-3} s^{-1}, the elastic modulus increased from 865.6 MPa for neat PLA to 973.2, 1129.2, and 1214.5 MPa for the 2, 4, and 6 wt% CNT compositions, corresponding to increases of approximately 12.4%, 30.5%, and 40.3%, respectively. At 1×10^{-4} s^{-1}, the corresponding increases were approximately 4.9%, 17.5%, and 22.3%. Similarly, for the ±45° line configuration at 1×10^{-3} s^{-1}, the elastic modulus increased by approximately 12.2%, 18.7%, and 29.3% with the addition of 2, 4, and 6 wt% CNT, respectively. The largest relative increases were observed for the ±45° specimens tested at 1×10^{-4} s^{-1}, where the modulus increased from 725.6 MPa for neat PLA to 1034.7, 1052.9, and 1158.1 MPa, corresponding to increases of approximately 42.6%, 45.1%, and 59.6%, respectively. Thus, in contrast to tensile strength, the elastic modulus exhibited a generally progressive increase with CNT content, demonstrating a clear stiffening effect of CNT incorporation.

The increase in stiffness was accompanied by a general decrease in strain at break, indicating reduced ductility following CNT incorporation. For the concentric specimens tested at 1×10^{-3} s^{-1}, the strain at break decreased by approximately 12.0%, 24.1%, and 31.2% for the 2, 4, and 6 wt% CNT compositions, respectively, compared with neat PLA. At 1×10^{-4} s^{-1}, the corresponding reductions were approximately 20.8%, 36.8%, and 29.5%. A similar behavior was observed for the ±45° line configuration. At 1×10^{-3} s^{-1}, the strain at break decreased by approximately 20.9%, 17.3%, and 25.7% for the 2, 4, and

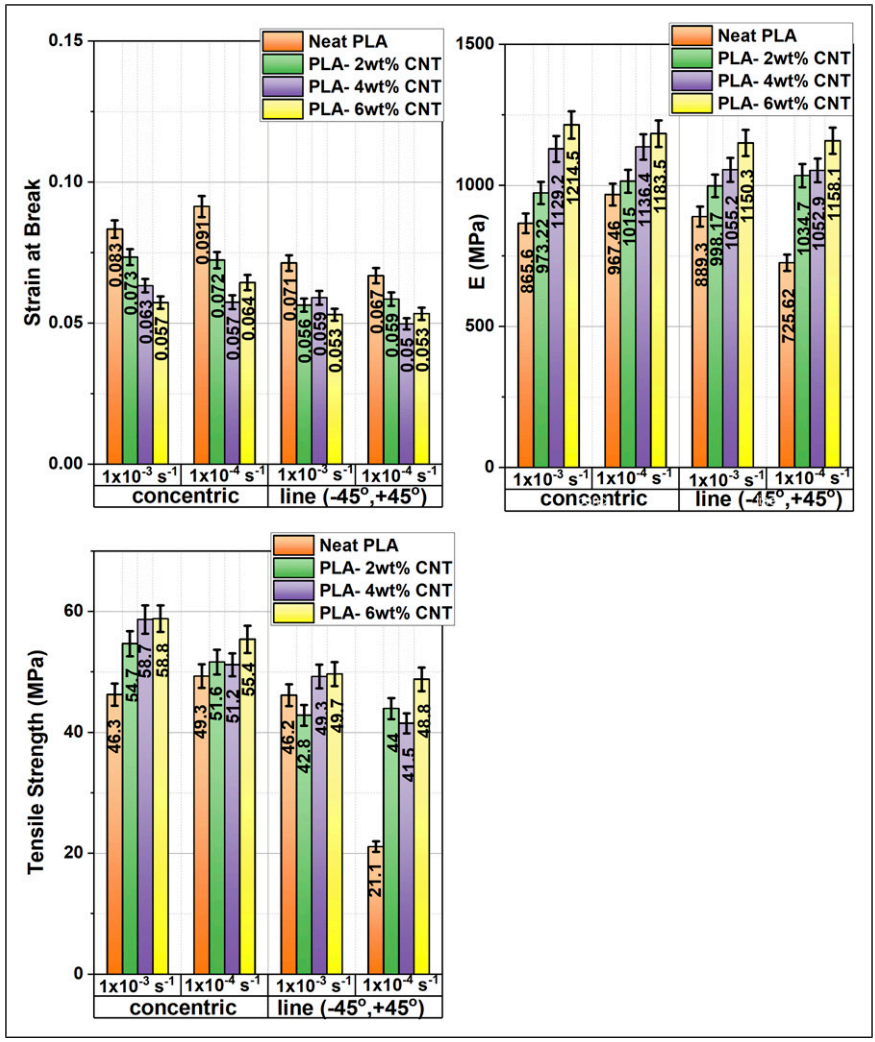


Figure 11. Influence of CNT content, raster orientation, and strain rate on the tensile performance of FFF-fabricated PLA–CNT nanocomposites.

6 wt% CNT compositions, respectively, whereas reductions of approximately 12.4%, 25.6%, and 20.1% were observed at 1×10^{-4} s^{-1}.

The differences observed between the ±45° line and concentric infill configurations indicate that the mechanical response is influenced by filament-path orientation and the resulting printing-induced anisotropy. Although shear flow during extrusion may promote preferential CNT alignment along the filament direction, CNT orientation was not directly characterized in the present study and its contribution cannot therefore be

quantified independently. In contrast, the ±45° raster orientation introduces a larger shear component between adjacent filaments, which reduces the effective tensile strength of the printed structures. Furthermore, the mechanical response of FFF-manufactured components is strongly influenced by interfilament bonding and internal porosity. The SEM observations and 2D pore area analysis presented in the previous section indicate that voids tend to form along the interfilament boundaries, which can act as stress concentration sites during tensile loading. Overall, the results demonstrate that both CNT reinforcement and printing architecture play critical roles in determining the tensile performance of FFF-fabricated PLA–CNT nanocomposites. A quantitative comparison with classical Rule of Mixtures predictions was not attempted because CNT orientation, dispersion state, interfacial load transfer, and the constituent properties required for a rigorous micromechanical analysis were not independently characterized in the present study.

Quasi-Static Loading–Unloading Behaviour

The strain rate dependent deformation recovery and energy dissipation behaviour of FFF-fabricated PLA and PLA–CNT nanocomposites during loading–unloading tests is presented in Figure 12. In loading–unloading tests performed at a strain level of 3%, PLA and PLA–CNT nanocomposite specimens exhibited approximately linear viscoelastic behavior. However, when the strain level was increased to 5%, a nonlinear viscoelastic response was observed.

An increase in strain rate resulted in an increase in both the strength and stiffness of the materials. As shown in Figure 13, the energy required for deformation at a strain rate of $1 \times 10^{-3}\ s^{-1}$ was higher than that required at $1 \times 10^{-4}\ s^{-1}$. When the strain rate increased from $1 \times 10^{-4}\ s^{-1}$ to $1 \times 10^{-3}\ s^{-1}$ at a strain level of 5%, the deformation energy of PLA and PLA–CNT nanocomposites increased by approximately 13.4%, 2.9%, 26.1%, and 9.5% for neat PLA, PLA–2 wt% CNT, PLA–4 wt% CNT, and PLA–6 wt% CNT, respectively. These results indicate that the mechanical response of PLA-based nanocomposites is sensitive to strain rate. At higher strain rates, the molecular mobility of polymer chains becomes restricted and the time available for molecular rearrangement decreases. As a result, the molecular resistance increases and the material exhibits a stiffer mechanical response. Consequently, elastic recovery after unloading becomes lower at higher strain rates.

The hysteresis loops obtained from the loading–unloading cycles reveal that energy dissipation is higher at lower strain rates. This behavior can be attributed to the greater mobility of polymer chains at lower deformation rates, which allows more internal energy dissipation through viscoelastic mechanisms. The addition of CNT increases the stiffness of the PLA matrix, leading to higher stored and recovered strain energy densities. As shown in Figure 13, both the stored strain energy density (U_loading) and the recovered strain energy density (U_unloading) increase with increasing CNT content. In contrast, the dissipated energy density (U_diss) generally decreases with increasing CNT content, indicating a reduction in viscoelastic energy loss. These results demonstrate that CNT reinforcement enhances the stiffness and load-bearing capability of PLA-

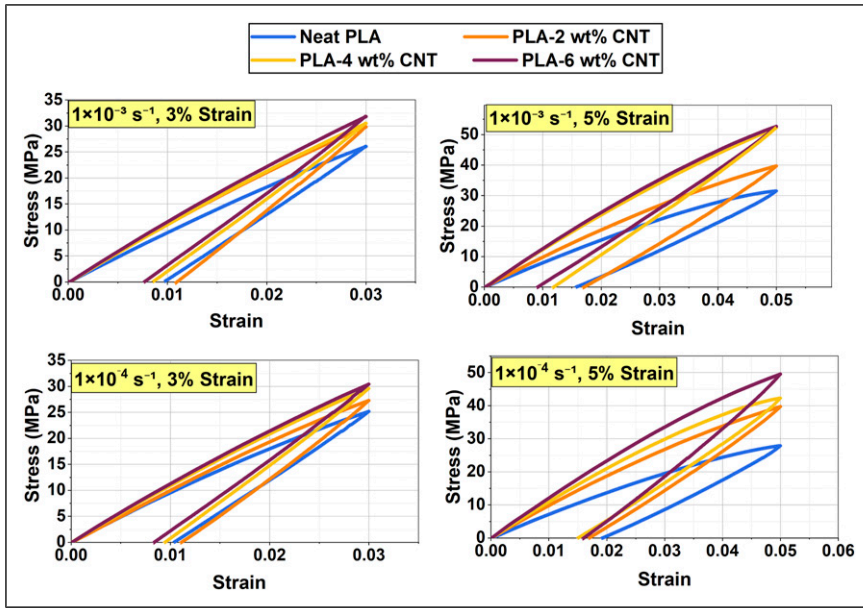


Figure 12. Quasi-static loading–unloading stress–strain response of FFF-fabricated PLA–CNT nanocomposites at different strain rates and maximum strain levels.

based nanocomposites while reducing the viscoelastic energy dissipation during loading–unloading deformation.

The strain-energy results indicate that CNT reinforcement primarily affected the balance between stored, recovered, and dissipated energy rather than simply increasing energy dissipation. In general, both the loading energy density ($U_{loading}$) and the recovered energy density ($U_{unloading}$) increased with CNT incorporation, particularly at the 5% maximum strain level. In contrast, the dissipated energy density (U_{diss}) generally decreased with CNT addition, especially at the lower strain rate of 1×10^{-4} s^{-1}. This behavior indicates that a greater fraction of the mechanical work supplied during loading was recovered during unloading in the CNT-reinforced specimens. Therefore, the present results should not be interpreted as an improvement in energy dissipation; rather, CNT reinforcement modified the energy-partitioning behavior of PLA toward increased recoverability and reduced irreversible or time-dependent deformation. This response is consistent with the intended application context of the present study, where dimensional stability and resistance to creep are more desirable than high energy dissipation.

Creep Behaviour

When the required instantaneous load to reach the desired stress level is applied, rapid deformation occurs due to elastic deformation and instantaneous creep. As shown in Figure 14, specimens reinforced with CNT exhibit lower total creep deformation

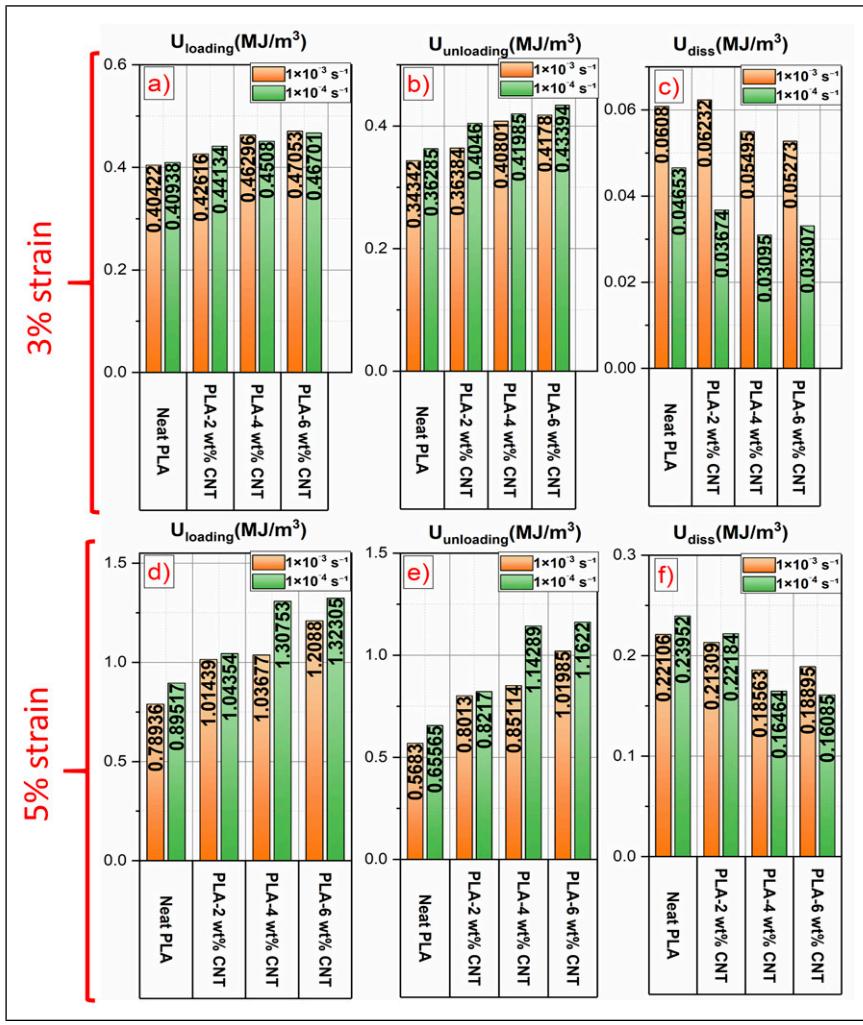


Figure 13. Strain energy densities of FFF-fabricated PLA–CNT nanocomposites at different strain rates and strain levels: (a–c) stored strain energy density ($U_{loading}$), recovered strain energy density ($U_{unloading}$), and dissipated energy density (U_{diss}) obtained at 3% strain; (d–f) corresponding results obtained at 5% strain.

compared to neat PLA specimens without nano-fillers. The creep compliance curves indicate that CNT reinforcement improves the creep resistance of PLA-based nanocomposites. CNT incorporation generally reduced the overall creep compliance of PLA, indicating improved resistance to time-dependent deformation. The reduction became more pronounced up to 4 wt% CNT, for which the lowest creep compliance values were observed. At 6 wt% CNT, a slight increase in creep compliance was observed relative to

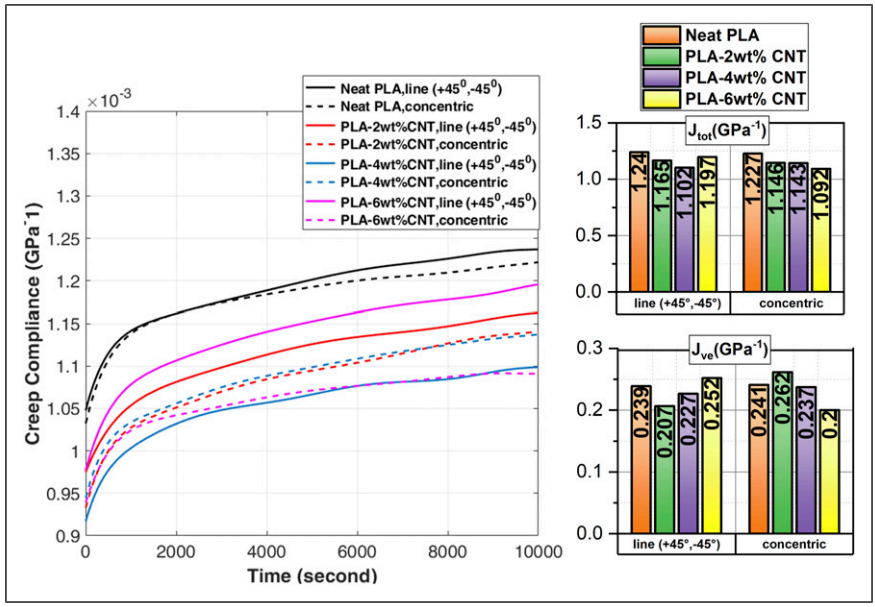


Figure 14. Creep behavior of FFF-fabricated PLA–CNT nanocomposites with different raster orientations.

the 4 wt% composition, indicating that the effect of CNT content was not strictly monotonic. This behavior may be related to changes in CNT dispersion, interfacial load transfer, or local microstructural heterogeneity at higher filler contents. These results are also consistent with the tensile and loading–unloading test results, indicating that CNT reinforcement enhances the stiffness and load-bearing capability of PLA-based nanocomposites. Although slight deviations may occur due to CNT agglomeration or insufficient interfacial adhesion, the overall trend clearly demonstrates that CNT reinforcement has a positive effect on the creep performance of PLA nanocomposites.

The ±45° raster specimens generally exhibited higher creep compliance than the concentric specimens, indicating a greater contribution of time-dependent deformation in the off-axis filament architecture. Similar orientation-dependent creep behavior has been reported for conventional polymer-matrix composites. Gupta and Raghavan[46] reported increasing creep compliance with increasing off-axis loading angle in woven polymer composites and attributed this behavior to the increasing contribution of creep deformation in the polymer matrix. Likewise, Kawai and Masuko[47] demonstrated pronounced time-dependent deformation in angle-ply carbon/epoxy laminates, including ±45° configurations. Although the filament architecture of FFF-fabricated specimens differs from that of conventional laminated composites, the present results are consistent with the general observation that off-axis architectures promote a greater contribution from matrix-dominated viscoelastic deformation.

The reduced creep compliance and improved recovery observed with CNT reinforcement suggest greater resistance to time-dependent deformation under sustained contact loads. This response is particularly relevant to sliding conditions, where progressive deformation can modify the real contact area and influence both friction and material removal. The following tribological results were therefore evaluated in relation to the preceding mechanical and viscoelastic findings.

Wear Behaviour

The wear test results are depicted in Figure 15. Results at room temperature indicate that the addition of CNT significantly improves the wear resistance of PLA specimens. Compared to neat PLA, the wear rates of PLA–CNT nanocomposites decreased by approximately 21.8%, 25.6%, and 39% for 2 wt%, 4 wt%, and 6 wt% CNT additions for line infill pattern, respectively. The corresponding reductions for the grid pattern were 0.8%, 16.1%, and 18.5%, while those for the concentric pattern were 5.1%, 23.2%, and 30.8%. At 30°C, the effect of CNT addition became particularly pronounced for the line

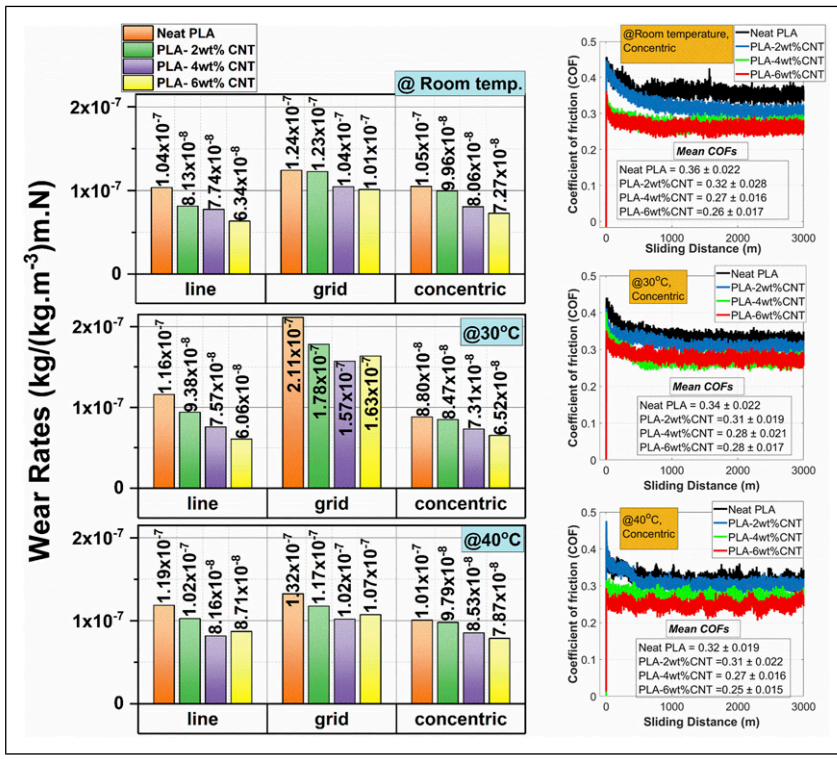


Figure 15. Wear rates and coefficient of frictions of FFF-fabricated PLA–CNT nanocomposites under different temperature conditions.

pattern, for which the wear rate decreased by approximately 19.1%, 34.7%, and 47.8% with 2, 4, and 6 wt% CNT, respectively. For the grid pattern, the corresponding reductions were 15.6%, 25.6%, and 22.7%, whereas reductions of 3.7%, 16.9%, and 25.9% were obtained for the concentric pattern. At 40°C, the line specimens showed wear-rate reductions of approximately 14.3%, 31.4%, and 26.8%, respectively. The corresponding reductions were 11.4%, 22.7%, and 18.9% for the grid pattern and 3.1%, 15.5%, and 22.1% for the concentric pattern. Overall, the influence of CNT content on wear resistance depended on both the infill architecture and test temperature, with the largest reduction observed for the 6 wt% CNT line specimen at 30°C. CNT incorporation generally lowered the friction coefficient, with the largest reductions occurring at the higher CNT contents. The temperature dependence was not strictly monotonic for every composition, indicating that the frictional response is governed by the combined effects of CNT content and contact temperature.

These results indicate that CNT reinforcement contributes to enhanced wear resistance, although the improvement is influenced by the internal structure of the printed specimens. Among the results, the best wear performance was generally obtained for specimens containing higher CNT contents. The improvement in wear resistance can be attributed to the reinforcing effect of CNT particles within the polymer matrix. CNTs increase the stiffness of the material and improve the load-bearing capability of the surface during sliding contact.

In grid infill structures, voids exist between adjacent filaments. During sliding, detached CNT particles may accumulate in these voids and act as third-body abrasive particles, which can locally increase abrasive wear and reduce the improvement in wear resistance. In contrast, specimens produced with line (±45°) raster orientations exhibit a more compact internal structure. During fused deposition modeling, the filaments are deposited at alternating angles of −45° and +45° in successive layers, which increases the rigidity of the printed structure and reduces the overall porosity. Consequently, the wear resistance of these specimens becomes higher. Temperature also plays an important role in the wear mechanism. At elevated temperatures, the dominant wear mechanism gradually shifts from abrasive wear to adhesive wear. Although particles may detach during sliding, they tend to soften due to frictional heating and therefore cannot remain as hard abrasive particles capable of significantly increasing the wear rate.

Furthermore, the increase in temperature may reduce the effective porosity within the printed structure, preventing detached particles from being trapped in internal voids. As a result, the contribution of abrasive wear decreases. In addition, CNT reinforcement can exhibit a lubricating effect at the sliding interface, which contributes to a reduction in the friction coefficient. The friction coefficient measurements support this interpretation. At room temperature, the friction coefficient decreased by approximately 11.1%, 24.7%, and 26.8% for PLA specimens containing 2 wt%, 4 wt%, and 6 wt% CNT, respectively. This reduction can be attributed to the lubricating behaviour of CNT particles and the improved load distribution at the sliding interface. Overall, the results demonstrate that CNT reinforcement significantly enhances the tribological performance of PLA-based nanocomposites by reducing both wear rate and friction coefficient.

Conclusions

This study provides an integrated assessment of the mechanical, loading–unloading, creep, and tribological behavior of FFF-fabricated PLA/CNT nanocomposites. Rather than considering these responses independently, the experimental results demonstrate that CNT incorporation modifies several interconnected aspects of the material response, including stiffness, deformation recovery, time-dependent creep, friction, and wear. The results therefore extend the assessment of PLA/CNT nanocomposites beyond conventional tensile characterization and provide a broader understanding of their behavior under sustained and sliding-contact loading conditions.

CNT incorporation generally increased the stiffness of the printed PLA and altered the balance between recovered and dissipated strain energy during loading–unloading deformation. The creep results further showed that both CNT content and filament-path architecture influence time-dependent deformation, with the ±45° raster configuration exhibiting higher creep compliance than the concentric architecture. This orientation-dependent response highlights the importance of considering printing-induced anisotropy when evaluating the long-term performance of FFF-fabricated components.

The tribological results showed that CNT addition generally reduced wear rate and friction, although the magnitude of these changes depended on infill architecture and test temperature. SEM-based 2D pore analysis also indicated lower mean pore area and pore area fraction for the CNT-containing specimens, with the lowest values observed at an intermediate CNT content. However, these microstructural changes should be interpreted as the combined outcome of material composition and FFF processing conditions rather than being attributed exclusively to CNT reinforcement.

Overall, the findings show that the performance of FFF-fabricated PLA/CNT nanocomposites cannot be assessed solely from static tensile properties. The practical implication of these findings is that CNT content and filament-path architecture should not be selected solely on the basis of tensile strength; they should be considered together with creep resistance, deformation recovery, friction, and wear when designing FFF-fabricated PLA/CNT components for sustained-loading and sliding-contact applications. By linking static mechanical response, time-dependent deformation, and tribological performance within the same material system, this study provides a more application-oriented basis for the design and evaluation of such components. Beyond experimental characterization, advanced numerical and multiphysics approaches have increasingly been employed to investigate coupled thermal, mechanical, and transport phenomena in complex nanoscale material systems.[48,49] Such approaches could be useful in future studies for linking CNT orientation, printing-induced anisotropy, temperature-dependent deformation, and local contact behavior in FFF-fabricated PLA/CNT nanocomposites. Future work should also focus on quantitative characterization of CNT orientation and dispersion, three-dimensional pore morphology, and micromechanical modelling of printing-induced anisotropy to establish more direct structure–property relationships.

Author contributions

Kamil Feratoğlu: Conceptualization, Methodology, Investigation, Formal analysis, Visualization, Writing – original draft, Writing – review & editing.
İlyas İstif: Supervision, Validation, Resources, Writing – review & editing.

Declaration of Conflicting Interests

The authors declared no potential conflicts of interest with respect to the research, authorship, and/or publication of this article.

Funding

The authors received no financial support for the research, authorship, and/or publication of this article.

Ethical Considerations

Ethical approval was not required for this study because it did not involve human participants or animals.

ORCID iD

Kamil Feratoğlu https://orcid.org/0000-0002-2280-6529

Data Availability Statement

The datasets generated and analyzed during the current study are available from the corresponding author on reasonable request.

References

1. Garzon-Hernandez S, Garcia-Gonzalez D, Jérusalem A, et al. Design of FDM 3D printed polymers: an experimental-modelling methodology for the prediction of mechanical properties. *Mater Des* 2020; 188: 108414. https://doi.org/10.1016/j.matdes.2019.108414
2. Hsueh M-H, Lai C-J, Wang S-H, et al. Effect of printing parameters on the thermal and mechanical properties of 3D-Printed PLA and PETG, using fused deposition modeling. *Polymers* 2021; 13: 1758. https://doi.org/10.3390/polym13111758
3. Rentería-Baltiérrez FY, Puente-Córdova JG, Hernández-Ramos JM, et al. Effect of 3D printing parameters on the viscoelastic behavior of acrylonitrile butadiene styrene: fractional calculus modeling and statistical optimization. *Polymers* 2025; 17: 1650. https://doi.org/10.3390/polym17121650
4. Tao Y, Kong F, Li Z, et al. A review on voids of 3D printed parts by fused filament fabrication. *J Mater Res Technol* 2021; 15: 4860–4879. https://doi.org/10.1016/j.jmrt.2021.10.108
5. Nguyen KQ, Vuillaume PY, Hu L, et al. Effect of in situ thermal treatment on interlayer adhesion of 3D printed polyetherimide (PEI) parts produced by fused deposition modeling (FDM). *Mater Today Commun* 2024; 39: 108588. https://doi.org/10.1016/j.mtcomm.2024.108588

6. Samy AA, Golbang A, Harkin-Jones E, et al. Finite element analysis of residual stress and warpage in a 3D printed semi-crystalline polymer: effect of ambient temperature and nozzle speed. *J Manuf Process* 2021; 70: 389–399. https://doi.org/10.1016/j.jmapro.2021.08.054
7. Omer MAE, Shaban IA, Mourad A-H, et al. Advances in interlayer bonding in fused deposition modelling: a comprehensive review. *Virtual Phys Prototyp* 2025; 20: e2522951. https://doi.org/10.1080/17452759.2025.2522951
8. Abbas I, Hobiny A, Alshehri H, et al. Analysis of thermoelastic interaction in a polymeric orthotropic medium using the finite element method. *Polymers* 2022; 14: 2112. https://doi.org/10.3390/polym14102112
9. Waseem M, Salah B, Habib T, et al. Multi-response optimization of tensile creep behavior of PLA 3D printed parts using categorical response surface methodology. *Polymers* 2020; 12: 2962. https://doi.org/10.3390/polym12122962
10. Stankevics L, Bulderberga O, Sevcenko J, et al. Viscoelastic creep of 3D-Printed polyethylene terephthalate glycol samples. *Polymers* 2025; 17: 2075. https://doi.org/10.3390/polym17152075
11. Salazar-Martín AG, García-Granada AA, Reyes G, et al. Time-dependent mechanical properties in polyetherimide 3D-Printed parts are dictated by isotropic performance being accurately predicted by the generalized time hardening model. *Polymers* 2020; 12: 678. https://doi.org/10.3390/polym12030678
12. Feratoğlu K, İstif İ, Gümüş ÖY, et al. Effect of carbon nanotube reinforcement on creep and recovery behavior of additively manufactured polymers: an experimental and prediction study. *Arabian J Sci Eng* 2024. DOI: 10.1007/s13369-024-08855-4, Epub ahead of print 13.
13. Ravindiran R, Malkapuram D, Arunachalam KP, et al. Enhancing tribological performance of 3D-Printed novel Hybrid Poly(Lactic) acid composites through synergistic reinforcement of carbon nanotubes and Delonix regia pod ash. *J Appl Polym Sci* 2026; 143: e70130. https://doi.org/10.1002/app.70130
14. Perez DB, Celik E and Karkkainen RL. Investigation of interlayer interface strength and print morphology effects in fused deposition modeling 3D-Printed PLA. *3D Print Addit Manuf* 2021; 8: 23–32. https://doi.org/10.1089/3dp.2020.0109
15. Sanusi OM, Médéric P, Benelfellah A, et al. Rheological and nonlinear mechanical behavior of PLA/MWCNT/MMT nanocomposites under cyclic loading: influence of hybrid filler concentration and dispersion. *Polym Compos* 2026; 47: 5518–5527. https://doi.org/10.1002/pc.70507
16. Hassanzadeh-Aghdam MK, Mahmoodi MJ and Ansari R. Creep performance of CNT polymer nanocomposites -An emphasis on viscoelastic interphase and CNT agglomeration. *Composites, Part B Eng* 2019; 168: 274–281. https://doi.org/10.1016/j.compositesb.2018.12.093
17. Ansari R and Hassanzadeh-Aghdam MK. Micromechanical investigation of creep-recovery behavior of carbon nanotube-reinforced polymer nanocomposites. *Int J Mech Sci* 2016; 115–116: 45–55. https://doi.org/10.1016/j.ijmecsci.2016.06.005
18. Saadi OW, Schiffer A and Kumar S. Piezoresistive behavior of DLP 3D printed CNT/polymer nanocomposites under monotonic and cyclic loading. *Int J Adv Manuf Technol* 2023; 126: 1965–1978. https://doi.org/10.1007/s00170-023-11123-8

19. Kontou E, Charitos I and Drougkas A. Modeling the fundamental viscoelastic properties of polylactic acid (PLA) and PLA/nanocomposites in a unified manner. *Nanomaterials* 2024; 14: 1116. https://doi.org/10.3390/nano14131116
20. Sandanamsamy L, Harun WSW, Ishak I, et al. A comprehensive review on fused deposition modelling of polylactic acid. *Progr Addit Manuf* 2023; 8: 775–799. https://doi.org/10.1007/s40964-022-00356-w
21. Li Y, Huang L, Wang X, et al. Blending and functionalisation modification of 3D printed polylactic acid for fused deposition modeling. *Rev Adv Mater Sci*; 62. DOI: 10.1515/rams-2023-0140, Epub ahead of print 1 January 2023.
22. Bardot M and Schulz MD. Biodegradable Poly(Lactic acid) nanocomposites for fused deposition modeling 3D printing. *Nanomaterials* 2020; 10: 2567. https://doi.org/10.3390/nano10122567
23. Al AA, Chakrabarti D and Trindade B. Fused filament fabricated poly(lactic acid) parts reinforced with short carbon fiber and graphene nanoparticles with improved tribological properties. *Polymers* 2023; 15: 2451. https://doi.org/10.3390/polym15112451
24. Sztorch B, Dydek K, Frydrych M, et al. Improved impact strength and thermal resistance of polylactide composites reinforced with CNT and polysiloxanes. *Polym Adv Technol* 2025; 36: e70409. https://doi.org/10.1002/pat.70409
25. Karabudak F. Comparative mechanical and thermal performance of Graphene- and silver nanoparticle-reinforced PLA fabricated by FDM 3D printing. *Polymers* 2026; 18: 1494. https://doi.org/10.3390/polym18121494
26. Plamadiala I, Croitoru C, Pop MA, et al. Enhancing polylactic acid (PLA) performance: a review of additives in fused deposition modelling (FDM) filaments. *Polymers* 2025; 17: 191. https://doi.org/10.3390/polym17020191
27. Zotti A, Paduano T, Napolitano F, et al. Fused deposition modeling of polymer composites: development, properties and applications. *Polymers* 2025; 17: 1054. https://doi.org/10.3390/polym17081054
28. Rahmatabadi D, Yousefi MA, Shamsolhodaei S, et al. 4D printing of polyethylene glycol-grafted carbon nanotube-reinforced polyvinyl chloride–polycaprolactone composites for enhanced shape recovery and thermomechanical performance. *Adv Intell Syst* 2025; 7: 2500113. https://doi.org/10.1002/aisy.202500113
29. Vidakis N, Petousis M, Kourinou M, et al. Additive manufacturing of multifunctional polylactic acid (PLA)—Multiwalled carbon nanotubes (MWCNTs) nanocomposites. *Nanocomposites* 2021; 7: 184–199. https://doi.org/10.1080/20550324.2021.2000231
30. Wang P, Liu J, Yang L, et al. Poly(lactide)/poly(butylene adipate-*co*-terephthalate)/carbon nanotubes composites with robust mechanical properties, fatigue-resistance and dielectric properties. *Int J Biol Macromol* 2025; 295: 139464. https://doi.org/10.1016/j.ijbiomac.2025.139464
31. Rachaiah B, Puttaswamy JT, Nagaraju SB, et al. Investigation on the wear characteristics of 3D printed graphene-reinforced PLA composites. *Discov Mater* 2024; 4: 75. https://doi.org/10.1007/s43939-024-00152-z
32. Feratoğlu K and İstif İ. Effect of carbon nanotube reinforcement and porosity on mechanical and viscoelastic properties of polylactic acid in material extrusion additive manufacturing.

Proceedings of the 3rd International Congress on Engineering and Life Science (ICELIS 2023). ICELIS / Karadeniz Technical University, 2023, p. 102. Trabzon, Türkiye.
33. Thirugnanasambandam A, Amith SC, Santhosh S, et al. Mechanical performance of PLA-MWCNT nanocomposite developed by ecofriendly hybrid filament processing method for fused deposition modeling applications. *Polym Compos* 2025; 46: 15584–15597. https://doi.org/10.1002/pc.30141
34. Seligra PG, Lamanna M and Famá L. Promising PLA-functionalized MWCNT composites to use in nanotechnology. *Polym Compos* 2016; 37: 3066–3072. https://doi.org/10.1002/pc.23504
35. Younus MM, Naguib HM, Fekry M, et al. Pushing the limits of PLA by exploring the power of MWCNTs in enhancing thermal, mechanical properties, and weathering resistance. *Sci Rep* 2023; 13: 16588. https://doi.org/10.1038/s41598-023-43660-3
36. Wu D, Wu L, Zhang M, et al. Viscoelasticity and thermal stability of polylactide composites with various functionalized carbon nanotubes. *Polym Degrad Stabil* 2008; 93: 1577–1584. https://doi.org/10.1016/j.polymdegradstab.2008.05.001
37. Begum SR, Devan BA, Kavya S, et al. Study on pistachio shell filled PLA composites for FDM-based processing. *Sci Rep* 2025; 15: 38215. https://doi.org/10.1038/s41598-025-22006-1
38. Xia H, Wang Q, Li K, et al. Preparation of polypropylene/carbon nanotube composite powder with a solid-state mechanochemical pulverization process. *J Appl Polym Sci* 2004; 93: 378–386. https://doi.org/10.1002/app.20435
39. Villmow T, Pötschke P, Pegel S, et al. Influence of twin-screw extrusion conditions on the dispersion of multi-walled carbon nanotubes in a poly(lactic acid) matrix. *Polymer* 2008; 49: 3500–3509. https://doi.org/10.1016/j.polymer.2008.06.010
40. Wang L, Qiu J, Sakai E, et al. The relationship between microstructure and mechanical properties of carbon nanotubes/polylactic acid nanocomposites prepared by twin-screw extrusion. *Compos Part Appl Sci Manuf* 2016; 89: 18–25. https://doi.org/10.1016/j.compositesa.2015.12.016
41. Le T-H, Le V-S, Dang Q-K, et al. Microstructure evaluation and thermal–mechanical properties of ABS matrix composite filament reinforced with multi-walled carbon nanotubes by a single screw extruder for FDM 3D printing. *Appl Sci* 2021; 11: 8798. https://doi.org/10.3390/app11198798
42. Tunçel O, Tüfekci K and Kahya Ç. Multi-objective optimization of 3D printing process parameters using gray-based taguchi for composite PLA parts. *Polym Compos* 2024; 45: 12870–12884. https://doi.org/10.1002/pc.28674
43. Naveed N. Investigating the material properties and microstructural changes of fused filament fabricated PLA and Tough-PLA parts. *Polymers* 2021; 13: 1487. https://doi.org/10.3390/polym13091487
44. Gong K, Luo H, Feng D, et al. Wear of Ni3Al-based materials and its chromium-carbide reinforced composites. *Wear* 2008; 265: 1751–1755. https://doi.org/10.1016/j.wear.2008.04.038
45. Fu T-H and Li D-R. Real-time process monitoring and error correction in material extrusion-based additive manufacturing via multi-output machine learning. *J Manuf Process* 2025; 152: 638–656. https://doi.org/10.1016/j.jmapro.2025.08.025

46. Gupta A and Raghavan J. Creep of plain weave polymer matrix composites under on-axis and off-axis loading. *Compos Part Appl Sci Manuf* 2010; 41: 1289–1300. https://doi.org/10.1016/j.compositesa.2010.05.013
47. Kawai M and Masuko Y. Creep behavior of unidirectional and angle-ply T800H/3631 laminates at high temperature and simulations using a phenomenological viscoplasticity model. *Compos Sci Technol* 2004; 64: 2373–2384. https://doi.org/10.1016/j.compscitech.2004.04.004
48. Shahid A, Huang HL, Bhatti MM, et al. Numerical computation of magnetized bioconvection nanofluid flow with temperature-dependent viscosity and arrhenius kinetic. *Math Comput Simulat* 2022; 200: 377–392. https://doi.org/10.1016/j.matcom.2022.04.032
49. Askar S, Abouelregal AE, Marin M, et al. Photo-thermoelasticity heat transfer modeling with fractional differential actuators for stimulated nano-semiconductor media. *Symmetry* 2023; 15: 656. https://doi.org/10.3390/sym15030656